BACHELOR

Optical emission spectroscopy on an atmospheric pressure dielectric barrier discharge in CO2

van der Schans, M.

Award date:
2012

Link to publication

Optical emission spectroscopy on an atmospheric pressure dielectric barrier discharge in CO_2

M. van der Schans
April 2012   PMP 12-04

Supervisors:

Dipl.-Phys. F. Brehmer
dr. S. Welzel
dr. R. Engeln

Abstract

A new way of producing clean energy on a large scale is required as the global energy demand grows and the fossil fuel resources are being depleted. Solar energy, one of the largest exploitable sustainable energy sources, will be essential in transitioning away from fossil fuels [1]. Through CO_2 conversion solar energy can be stored in chemical bonds. The dissociation of CO_2 is known to be the process limiting step. A dielectric barrier discharge (DBD) is considered to effectuate the dissociation, as high dissociation energy efficiencies are reported for non-equilibrium plasmas [2]. Optical emission spectroscopy (OES) is used on an atmospheric pressure DBD in CO_2, N_2 and mixtures of these two gases to characterise a new setup and to prepare further studies on the plasma-assisted dissociation of CO_2. The dominant peaks in the emission spectra of pure CO_2 plasmas were attributed to CO_2^+, while the origin of the lower intensity bands in the region above 425 nm is still unknown. Features of N_2, N_2^+ and NO were observed in the spectra from pure N_2 plasma. When CO_2 was mixed with N_2, the N_2 emission bands remained dominant in the spectrum. Furthermore the influence of the applied voltage and frequency, and thus the injected power, on the emission was studied. No qualitative changes in the spectra were observed while varying these parameters.

Contents

1. Introduction

1.1. Background and Motivation

The supply of clean and sustainable energy is perhaps one of the main scientific challenges of the 21st century, as the global energy consumption is projected to keep rising [3]. Fossil fuels could in principle still meet the growing demand of energy during this century [1]. However, the utilisation of fossil fuels contributes heavily to the emission of carbon dioxide (CO_2). An excess of CO_2 gases in the atmosphere is believed to be the primary cause of global warming [4]. Novel large-scale carbon-neutral energy production will be required to restrain the CO_2 levels in the atmosphere, and to keep up with the increasing demand of energy in the further future. Solar energy is a sustainable energy source with great potential to replace fossil fuels: the sun provides the earth with more energy in 1 hour than is consumed by all humans in a year [1]. The utilisation of solar energy is therefore essential in transitioning away from fossil fuels [5].

Solar energy will have to be stored in order to become a major primary energy source, which also involves that it can be dispatched on demand to the consumer [1]. One of the main reasons is the varying incident radiation throughout the day, as illustrated by figure 1.1 [6]. A buffer for the night-time could be established during the daytime by storing the energy.
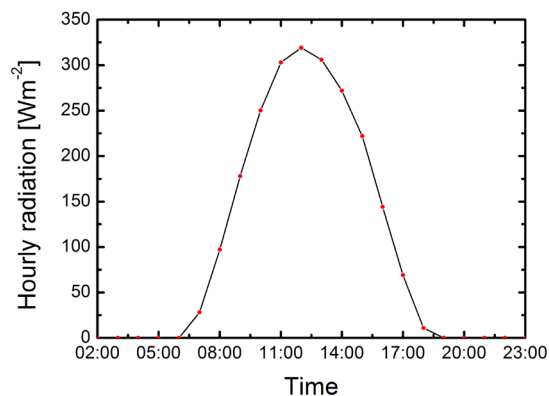

Figure 1.1: *The mean hourly radiation in March measured at De Bilt, Netherlands. The data originates from the Royal Netherlands Meteorological Institute (KNMI) [6].*

One approach is to store solar energy in chemical bonds. The conversion of CO_2 to hydrocarbon fuel is a process that could be used to this end and would lead to a carbon cycle as illustrated in figure 1.2. Nature provides us one famous example of such a carbon cycle: the photosynthetic process in plants, where glucose ($C_6H_{12}O_6$) is produced from CO_2 and water. More general, hydrocarbon fuels can be produced by the direct conversion of CO_2 (and H_2O) using photo-catalytic materials and sunlight. In this case the dissociation and the association step are performed at the same time. However, the photo-catalytic conversion of CO_2 currently has one major disadvantage regarding commercial feasibility: the highest reported energy efficiency so far is only 0.0148% [7]. The process-limiting step is the dissociation of CO_2.
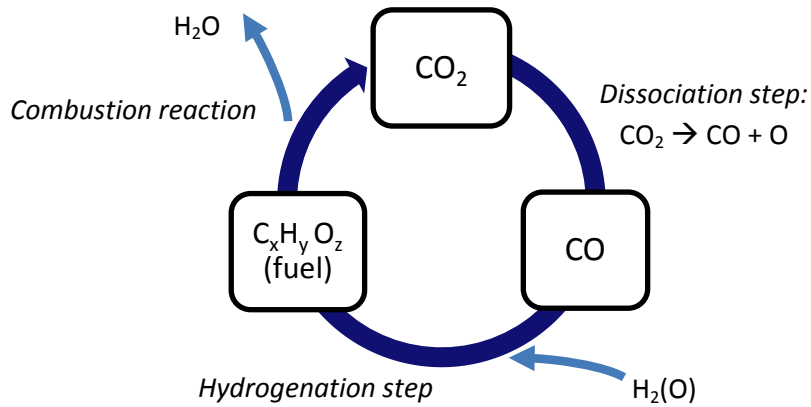
Figure 1.2: *The carbon cycle consists of three steps: CO_2 is dissociated to CO and O. Through hydrogenation a new hydrocarbon fuel can be produced from CO. In the combustion reaction CO_2 is produced from the hydrocarbon fuel.*

To surpass these limitations, plasma can be used to perform the dissociation step. So far dissociation energy efficiencies of up to 80% have been reported [2]. The highest efficiencies are typically achieved using non-equilibrium plasmas. Therefore a dielectric barrier discharge (DBD) is considered to effectuate the dissociation. To attain the necessary amounts of output, a flow-tube reactor is used. The DBD is a non-equilibrium plasma that can be operated at atmospheric pressure, with the advantage that no vacuum equipment is required. Another advantage of using a DBD is the ability to easily scale up both reactor volume and the number of reactors for industrial use [8]. The hydrogenation process could be performed successively after the dissociation process in either a plasma or using conventional techniques. With the two steps separated, they can be both optimised independently.

1.2. Project Goal and Description

The goal of this project is to set up an in-situ optical emission diagnostic for an atmospheric pressure dielectric barrier discharge in CO_2, N_2 and mixtures of these gases. Experiments with CO_2 as well as N_2 are performed to characterise a new setup and to prepare further studies on the dissociation of CO_2 in such plasmas.

The plasma is contained in a parallel plate flow reactor that allows direct optical access to the discharge. By changing the frequency and amplitude of the applied voltage, and thus the power transferred into the plasma, different process conditions can be obtained. The effects of changing these conditions are studied by mutual comparison of the spectra. Species present in the plasma are identified by comparing the measured spectra with literature. For this identification two spectrometers are used and calibrated: this involves both spectral calibration as well as relative intensity calibration using a tungsten ribbon lamp with a known spectral density.

2. Theory

In this chapter the theory required to understand the experimental setup and the results are presented. Molecular energy levels and electronic transitions are discussed in the first two sections respectively. Then, several dissociation mechanisms of CO_2 in plasma are summarised. Since dielectric barrier discharges are used to perform the dissociation of CO_2 in this work, an outline of the relevant physics is given in the final part of this chapter.

2.1. Molecular Energy Levels

As with atoms, molecules can only occupy discrete energy states, and hence the energy can only change by a definite amount $\Delta E = E_2 - E_1$, where E_2 and E_1 are the energies associated with two different states. Besides the energy distribution in electronic states, polyatomic molecules also retain energy in rotational and vibrational motion due to its internal structure [9]. This leads to quantized vibrational and rotational states, in addition to the electronic states [10]. For the spacing between different energy levels it is found that [11]:

$$\Delta E_{electronic} \gg \Delta E_{vibrational} \gg \Delta E_{rotational} \tag{2-1}$$

The pure electronic, vibrational and rotational transitions also take place on different timescales of 10^{-8} s, 10^{-13} s and 10^{-10} s respectively [12]. The energies associated with the different kinds of motion can be decoupled. This independence of the different energies is a result of the Born-Oppenheimer approximation [11]. The total energy E of a molecular state is then given by equation 2-2:

$$E = E_{electronic} + E_{vibrational} + E_{rotational} \tag{2-2}$$

The energy levels in a molecule are described quantum mechanically by the anharmonic oscillator. As opposed to the harmonic oscillator, the anharmonic oscillator takes bond breaking into account [13]. It follows from Schrödinger's equation that there is a finite amount of vibrational levels, and the energy spacing between vibrational levels decreases as the energy itself increases. For the rotational levels the same can be concluded. The molecular energy levels are schematically illustrated in figure 2.1. Dissociation may occur if the vibrational energy is large enough to break the nuclear bond [10]. The threshold energy for this to happen is the dissociation energy E_D.
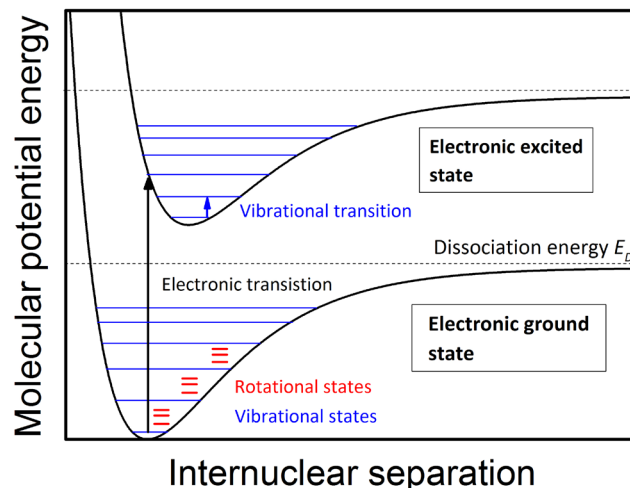
Figure 2.1: *Schematic representation of two electronic levels of a molecule.*

2.2. Molecular Emission Spectra

Each molecular state, consisting of a well-defined electronic, vibrational and rotational state, is associated with a well-defined total energy given by equation 2-2. When a radiative transition occurs from a higher energy state E_2 to a lower energy state E_1, a photon is emitted carrying the amount of energy ΔE:

$$\Delta E = E_2 - E_1 = \hbar\omega = \frac{2\pi\hbar c}{\lambda} \tag{2-3}$$

Each transition is thus associated with a specific frequency and wavelength. Since each molecule has a definite set of allowed transitions, the emission spectrum can be used to identify the molecule [10], [11]. Transitions between different electronic states require energies in the order of a few eV [9]. Consequently, the photons originating from electronic transitions mostly lie in the visible (VIS) and ultraviolet (UV) regions of the spectrum, as is shown in table 2.1.

Table 2.1: *Colour and wavelength are given for some energy values that a photon can attain during a transition. The colours are indications because different definitions of 'infrared' and 'ultraviolet' are used throughout literature [9].*

Colour	Wavelength [nm]	Energy [eV]
Infrared (IR)	>1000	<1.2
Red	700	1.7
Yellow	580	2.1
Blue	470	2.5
Ultraviolet (UV)	<300	>4.0

Since the energy spacing between vibrational and rotational states is much smaller than for electronic transitions (equation 2-1), the pure vibrational and pure rotational spectra lie in the far infrared region. In this work spectra are measured for wavelengths ranging from 200 to 700 nm. So, the peaks in those spectra arise from electronic transitions.

The set of allowed transitions results from the fact that not all possible transitions are permissible. A photon has an intrinsic (spin) angular momentum of $S = 1$, so the change in angular

momentum of the molecule must compensate for the spin carried away by the photon [9]. Selection rules for permissible transitions are derived from the conservation of angular momentum during the transition. In this work spectra will not be calculated. The identification of the measured spectra will be done by comparing them with literature. The exact details of all the selection rules are therefore not further discussed here, but can be referred to in [9], [10] or [11].

Spectral Line Broadening

A specific electronic transition in a molecule can be associated with different energies, depending on both the initial and the final vibrational and rotational state. A transition from the same initial electronic state to the same final electronic but with a different vibrational and rotational state will therefore introduce another peak in the spectrum. There are many possible vibrational and rotational transitions if an electronic transition occurs in a polyatomic molecule. Larger molecules also have a larger moment of inertia, which leads to closely spaced rotational levels. In that case, the spectral lines overlap and contribute to a broader band in the spectrum. In figure 2.2a a distinct peak as observed in an atomic spectrum is illustrated. Spectra of simple and small polyatomic molecules can often still be spectrally resolved into individual peaks as in figure 2.2b. Whereas for more complex and larger molecules overlapping of the spectral lines gives rise to a broad, nearly featureless, band as illustrated in figure 2.2c [11]. Since CO_2 is a linear triatomic molecule, its emission spectrum is expected to have features like the spectrum in figure 2.2b.
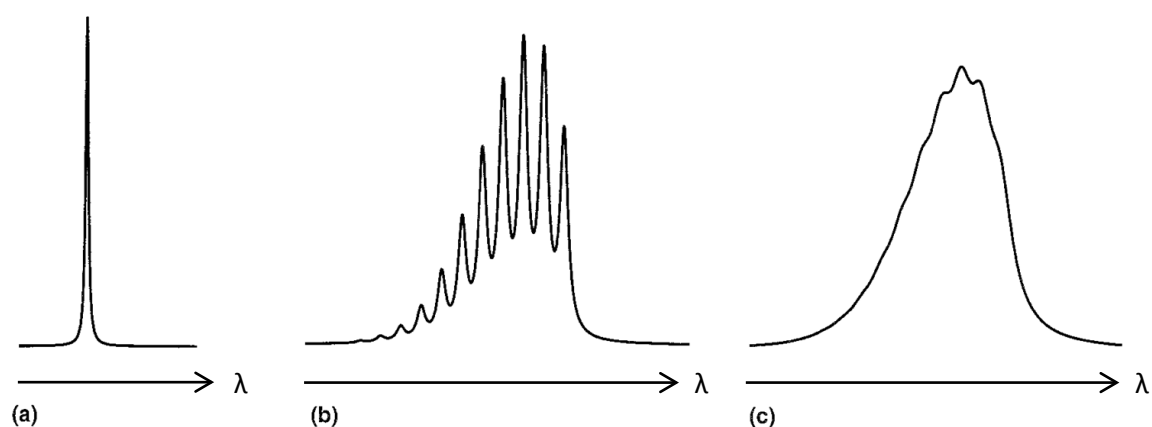

Figure 2.2: *A schematic spectrum is shown for an atom (a), for a small polyatomic molecule (b) and a large polyatomic molecule (c) [11].*

Another effect that needs to be considered is collision broadening. When a molecule approaches another, their interaction shifts the energy levels of both molecules. The collision of one molecule with another can affect the energy of the emitted photon and thereby create a broader band in the emission spectrum. When an inelastic collision occurs between two molecules, the excitation energy of the molecule is either partly or completely transferred into internal energy of the collision partner, or into translational energy of both molecules. This leads to a transition probability that is linearly dependent on the pressure and thus the line width in the emission spectrum is also pressure dependent [10]. The collision induced line broadening is often called pressure broadening. Its effects become more apparent at high pressures, such as atmospheric pressure, which is used for the experiments in this work.

Franck-Condon Principle

The relative intensities, as seen in figure 2.2b, can be explained by applying the Franck-Condon principle: before the molecule is excited, it is in the lowest vibrational state of the electronic ground state. The most probable position of the nuclei is at their equilibrium separation point, the point where the potential energy has its minimum, and thus the transition is most likely to occur when the nuclei are at this position. According to the Franck-Condon principle, the nuclei will stay in position during the transition. So, the transition can be represented by a vertical line up to the upper curve, as shown in figure 2.3. The vibrational level marked with the asterisk has the highest probability to be populated during the excitation while the internuclear distance remains the same. The wavefunction of the excited state has a maximum at the same internuclear separation and most closely resembles the wavefunction of the initial state. It can be concluded that this is the most probable final state for the excitation process. The emission line corresponding to this state will be the most intense, when the molecule decays back to the ground state. Of course the other vibrational states in the upper electronic level also have a probability to be populated, but to a lesser extent [9].
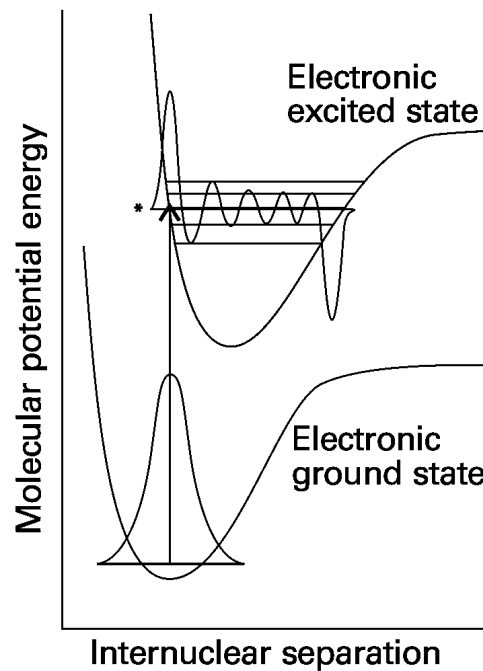

Figure 2.3: *Schematic representation of the Franck-Condon principle [9].*

2.3. CO$_2$ Dissociation in Plasma

The dissociation of molecules in plasma can occur through a number of different physical mechanisms under various plasma conditions. The dissociation of CO$_2$ in a thermal plasma results in maximum energy efficiencies of 40% [14]. Many types of plasma exist in conditions that are far from thermodynamic equilibrium. Non-equilibrium plasmas are often referred to as non-thermal plasmas [2]. An important advantage of non-equilibrium conditions is that the input energy is not necessarily expended in all degrees of freedom [14]. In the next section it is shown that this might lead to very high dissociation efficiencies.

Strictly speaking, the decomposition of CO_2 is an endothermic process and can be summarized by the following reaction [2], [14]:

$$CO_2 \rightarrow CO + \tfrac{1}{2}O_2, \quad \Delta H = 2.9 \text{ eV/molecule} \tag{2-4}$$
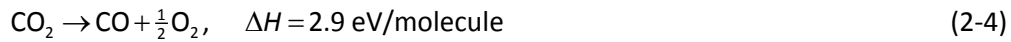
where ΔH is the reaction enthalpy per molecule. Process 2-4 starts with and is limited by the dissociation process given in 2-5.

$$CO_2 \rightarrow CO + O, \quad \Delta H = 5.5 \text{ eV/molecule} \tag{2-5}$$

The enthalpy of the total decomposition (2-4) is lower, because the formation enthalpy of O_2 from O is negative. Three possible mechanisms for CO_2 dissociation will be briefly discussed: dissociation by electronic excitation, dissociation by dissociative attachment of electrons and, finally, dissociation stimulated by vibrational excitation.

Dissociation by Electronic Excitation
Dissociation through electronic excitation in plasma is mostly related with direct electron impact and described by 2-6 [2].

$$e + CO_2 \rightarrow CO + O \tag{2-6}$$
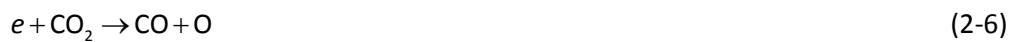
The electron energy required for this dissociation process is at least 8 eV, which exceeds the O=CO bond energy of 5.5 eV. The amount of energy transferred from plasma electrons to electronic excitation of CO_2 is also relatively low with values up to 25% at typical electron temperatures of 1 to 2 eV. These two reasons limit the energy efficiency of dissociation by means of electronic excitation. The highest reported dissociation energy efficiencies through electronic excitation are around 25% and are achieved in non-thermal discharges [15].

Dissociation by Dissociative Attachment of Electrons
Dissociation by dissociative attachments of electrons can be summarized by 2-7 [2].

$$e + CO_2 \rightarrow CO + O^- \tag{2-7}$$

While the energy threshold of this mechanism is lower than the threshold of 2-6, the dissociative attachment mechanism is limited by the loss of an electron, which has a high energy price ranging from 30 eV up to 100 eV. Therefore, this particular mechanism does not provide an energy efficient way to dissociate the CO_2 molecule.

Dissociation Stimulated by Vibrational Excitation
Vibrational excitation is the most effective channel for CO_2 dissociation in a plasma. This process is given by 2-8 [2].

$$CO_2{}^* \rightarrow CO + O \tag{2-8}$$

In 2-8 the asterisk indicates a vibrationally excited CO_2 molecule. This mechanism is effective for a couple of reasons: first, at electron temperatures typical for non-thermal discharges (a few eV), a large part of the discharge energy transfers from plasma electrons to vibrations of CO_2 molecules. Secondly, the vibrational-translational relaxation is relatively slow compared to the vibrational excitation by electron impact. This results in an increased population of the vibrational levels in

the electronic ground state of the CO_2 molecules. The plasma electrons mainly provide energy to the lower vibrational states. Higher vibrational states are obtained by vibrational-vibrational relaxation processes. This is called vibrational pumping. When vibrationally excited molecules have an energy exceeding the dissociation threshold E_D, as shown in figure 2.1, they are able to dissociate. Dissociation energy efficiencies of up to 80% could be achieved for non-thermal discharges in a subsonic flow of CO_2 by Legasov et al. [16]. However, it has to be mentioned that the authors made the assumption that the high efficiency is the result of the excitation of only one vibrational mode. This implies that all the input energy contributes to just one degree of freedom, while direct experiments show that at electron temperatures of a few eV only about 65% of the input energy can be used to excite the anti-symmetric vibrational mode [14]. So a further analysis on the exact efficiency and energy transfer are required in the future.

2.4. Dielectric Barrier Discharge

From the previous section the highest dissociation energy efficiencies are expected using a non-equilibrium plasma. A dielectric barrier discharge (DBD) is such a plasma. Using a DBD combines the advantages of non-equilibrium plasma with the possibility to work at atmospheric pressure [8]. In this section the principles and relevant physics regarding the DBD are shortly outlined.

Some basic DBD configurations are shown in figure 2.4 [8]. Each of the configurations in exists of two electrodes and at least one dielectric barrier in the gap between the electrodes. The dielectric does not pass any DC current and hence an alternating voltage is required for the operation of a DBD. The most common type of DBD at atmospheric pressure is filamentary. However, a DBD can also be operated in a glow-like diffuse mode [17]. In this work the filamentary mode is used.
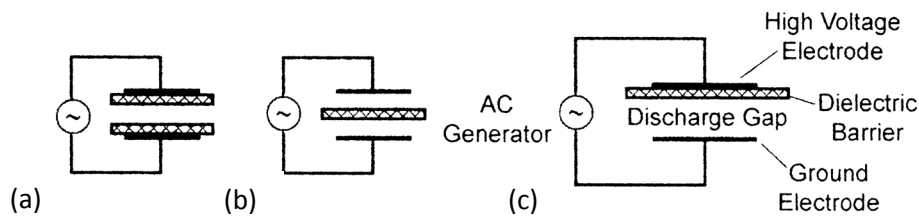

Figure 2.4: *Three basic DBD configurations: the first has a dielectric barrier located at each of the electrodes (a). This configuration is the one used in this work. The second has a single dielectric barrier located in between the electrodes (b). The last has a single dielectric barrier located at one of the electrodes (c) [8].*

The electric field in the gap accelerates electrons in the gas. The initial electron produces secondary electrons by direct ionisation and an electron avalanche will develop [18]. When such an electron avalanche is large enough, a streamer commences. This streamer bridges the gap in only a few nanoseconds and creates a channel of weakly ionised plasma. Electrons flow through the channel and subsequently negative charge is accumulated at the dielectric. The local electric field is reduced due to the charge building up at the dielectric, as shown in figure 2.5. Usually the set of local processes is called a microdischarge [18]. When the local electric field is completely cancelled, the flow of electrons is terminated and the microdischarge is quenched. The deposited charges still remain at the dielectric and when the polarity of the applied voltage is reversed they facilitate the formation of new microdischarges at the same location in the opposite spatial direction [8]. For this reason individual filaments are observed in this mode. The effect of the remaining charges from a previous microdischarge, which are not yet fully dissipated when the

next microdischarge occurs, is called the memory effect. After the initial breakdown a lower voltage can sustain the DBD due to the memory effect.
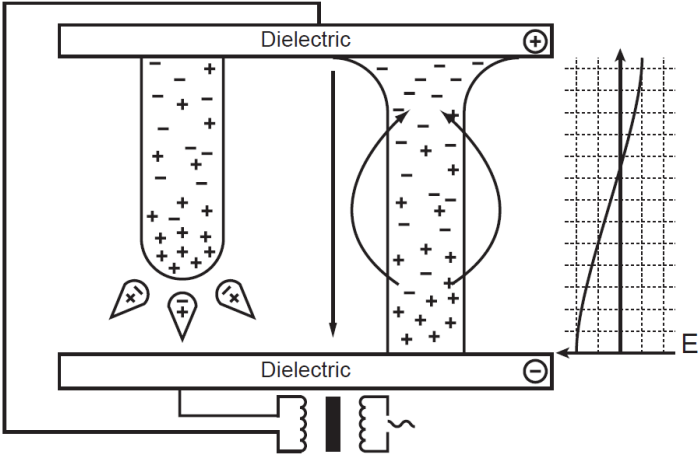

Figure 2.5: *On the left between the dielectric barriers the formation of a streamer is shown and on the right a plasma channel is illustrated. The arrow between the dielectric barriers indicates the applied external electric field. On the far right is a graph showing the local electric field caused by the microdischarge and its superposition with the external field [8].*

3. Experimental setup

In this chapter the different parts of the experimental setup are explained. In the first section the flow reactor, used for a controlled gas flow through the DBD, is discussed. Secondly, the electronics that were used to provide the voltage to ignite and maintain the DBD are shown. Lastly, the spectrometers employed to measure the optical emission originating from the plasma are presented.

3.1. Flow Reactor

The flow reactor is part of a quartz tube with two flat parallel plates in the middle. Two electrodes are attached to the outside of the quartz plates. With the quartz acting as dielectric barrier, a DBD in the configuration as shown in figure 2.4a is obtained. A sketch of the flow reactor tube is shown in figure 3.1a. Figure 3.1b shows a photograph of a N_2 plasma in the flow reactor and the lens system, which was used to collect the optical emission from the plasma.

(a)   (b)
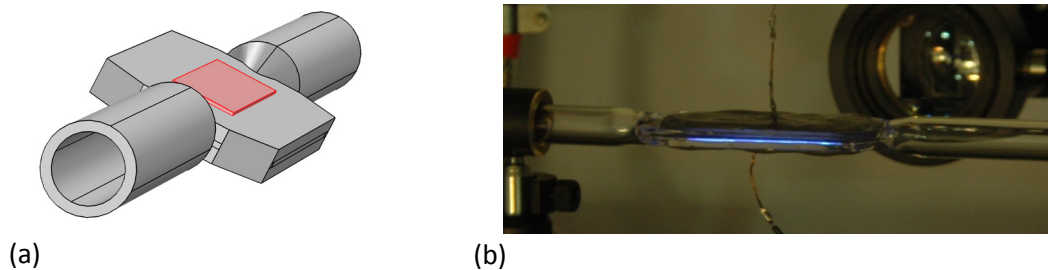
Figure 3.1: *A sketch of the flow reactor tube (a): the tubing and parallel plates are made of quartz and are shown in grey in the image. One of the electrodes is indicated in red. The discharge length is about 5 cm. On the right is a photograph of the setup (b): the tube with a CO_2 plasma is shown in the middle. In the upper right part of the picture are the lenses that are used to focus the emitted light on a fibre.*

The discharge gap between the dielectric quartz plates is 0.9 mm large. To ignite a DBD inside the tube at atmospheric pressure, alternating voltages of the order of 10 kV_{peak} are required. The electrodes are therefore covered with silicone to prevent discharges outside the tube. To create a controlled gas flow through the tube, the far sides are connected to a flow controller and gas supply on one side and to a pump and a Baratron gauge on the other side. Pure CO_2, pure N_2 and a combination of the two gases are used for the experiments. The valve of the flow controller and the valve after the pressure gauge give control over flow and pressure inside the tube. All experiments are performed at atmospheric pressure.

3.2. Electronics

To power the DBD in the flow reactor a generator and transformer are used to provide sinusoidal voltages in the kV range. Several capacitors are used to measure the power coupled into the plasma and to tune the resonance frequency of the electronic circuit. A schematic representation of the setup is shown in figure 3.2.
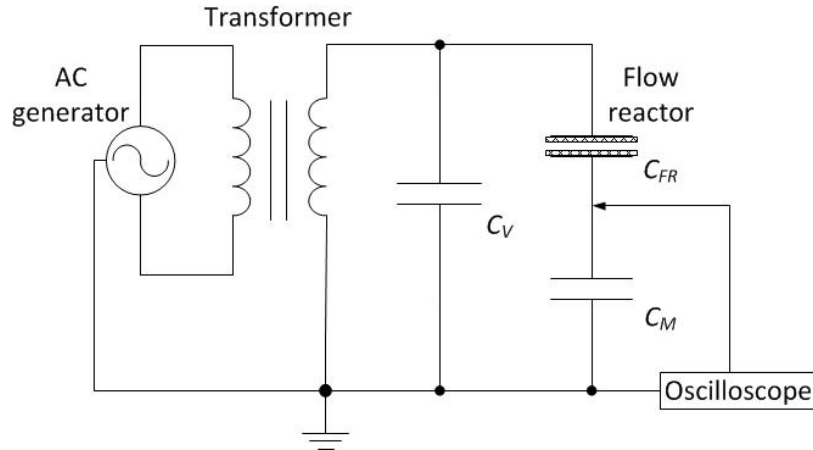
Figure 3.2: *Schematic representation of the electronics. The capacitance of the flow reactor C_{FR} is 2.2 pF. The value of C_M is 290 pF.*

An oscilloscope is used to measure the voltage over a capacitor C_M (290 pF) in series to the discharge. As C_M and C_{FR} (2.2 pF), the capacitance of the flow reactor, form a voltage divider, the high voltage signal can be calculated. The measured voltage and the calculated high voltage were used to determine the power that was coupled into the plasma via Lissajous figures [19].

The applied frequency is set to the resonance frequency of the system, which is determined by the capacitors and the inductance of the transformer coils. The parallel capacitor C_V is used to tune the resonance frequency of the circuit. The different capacities that were used for C_V and the resonance frequencies they impose on the circuit are listed in table 3.2.

Table 3.2: *Overview of the capacities used to change the electrical circuit's resonance frequency. In the last case the capacitor C_V is absent.*

Capacitance C_V [pF]	Resonance frequency f [kHz]
596	33,0
151	61,6
25	105
n/a	137

3.3. Spectrometers

The light emitted by the plasma is focussed on a fibre by two lenses. The fibre is connected to a spectrometer. Two spectrometers are used for the measurements. One with 1.4 nm spectral resolution (Ocean Optics USB 2000, estimated from the grating and the measured spectra) and one with higher resolution of up to 0.8 nm (Avantes AvaSpec-2048). The first is used to determine the range of interest in the spectra, while the latter is used to record spectra for further analysis.

For the Ocean Optics spectrometer a wavelength calibration was performed to match the pixels of its charge-coupled device (CCD) sensor with their corresponding wavelengths. This is done by measuring the spectra of several gas discharge lamps with known spectral lines. A detailed description of the process can be found in appendix A1.

Since the optical elements have wavelength dependent properties the emitted light from the plasma will be filtered. To obtain correct relative intensities in a measured spectrum, those effects

will have to be compensated for. This is done by comparing a measured tungsten ribbon lamp spectrum with its theoretical counterpart, the grey body radiator. Dividing the calculated (ideal) spectrum of the lamp by a measured spectrum gives a wavelength dependent correction function. Applying the correction to any measured spectrum yields correct relative intensities. Such a relative intensity calibration was performed for the Avantes spectrometer. A detailed discussion of the intensity calibration can be found in appendix A2.

4. Results

In this chapter the results of the measurements will be presented and briefly discussed. First the emission spectra of pure N_2 and pure CO_2 are analysed. Next, they are compared with the spectra of a plasma using a combination of the two gases. In the third section of this chapter the effects of different powers and resonance frequencies on the emission spectra are presented.

4.1. Identification of Emission Spectra

To identify the excited species present in the plasma, the peaks in the emission spectra are compared to values from 'The identification of molecular spectra' by Pearse & Gaydon [20]. A detailed description of the identification process for pure N_2 and pure CO_2 is given in appendix B.

Pure N_2 Emission Spectrum

Fourteen spectra were measured for pure N_2, all of them at a flow rate of 0.35 L/min. To identify the species in the plasma, the DBD was operated at an applied frequency of 105 kHz and an integration time of 50 ms was used. A sample spectrum encompassing the molecular band identification is shown in figure 4.1. The peaks in the pure N_2 emission spectrum mainly arise from the N_2 second positive transition system ($C^3\Pi_u - B^3\Pi_g$). A few features among the peaks of lower intensity do not match the second positive system and indicate that the N_2^+ first negative transition system ($B^2\Sigma_u^+ - X^2\Sigma_g^+$) is also present.
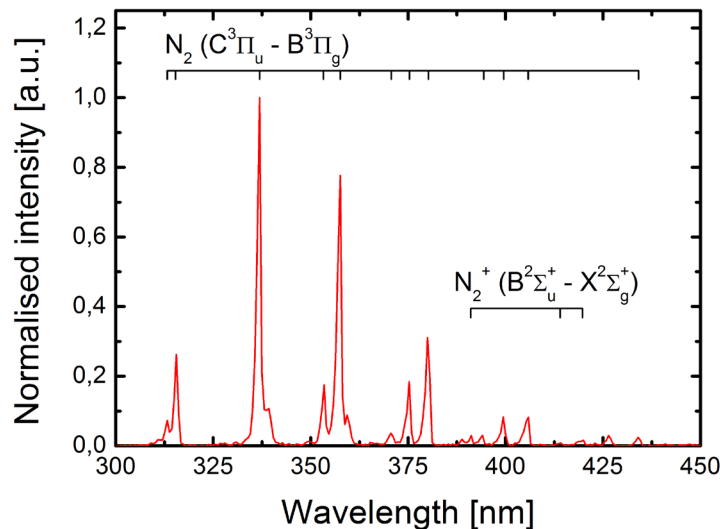
Figure 4.1: *This pure N_2 spectrum was recorded using an applied frequency of 105 kHz and an integration time of 50 ms. The peaks in the emission spectrum are mostly attributed to the N_2 second positive transition system. The N_2^+ first negative transition system is present to a small extent.*

When a longer integration time is used the high intensity peaks are saturated. However, the longer integration time makes additional structure in the wavelength region below 300 nm more apparent. The additional peaks, which are shown in figure 4.2, are attributed the NO γ system ($A^2\Sigma^+ - X^2\Pi$). Possible explanations for the observed NO peaks could be a leak in the system or H_2O contamination of the N_2 gas.
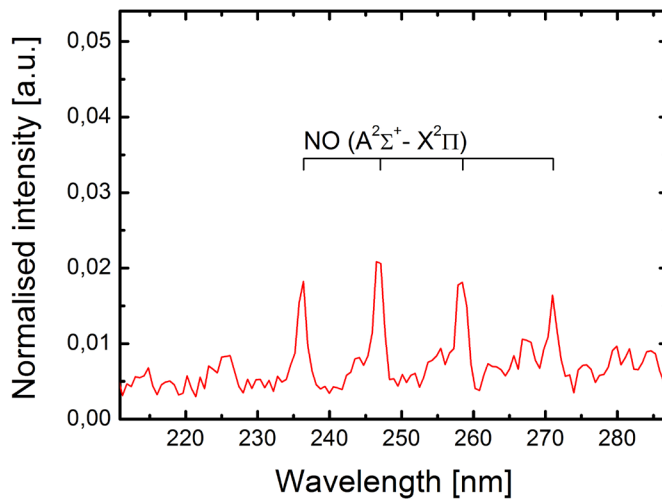
Figure 4.2: *Enlarged view of the lower wavelength region of the N_2 spectrum. Using longer integration times four NO peaks became apparent in the region between 230 and 280 nm.*

Pure CO_2 Emission Spectrum

For pure CO_2, six spectra were recorded, all of them at a flow rate of 0.32 L/min. The spectrum measured at an applied frequency of 105 kHz was used for identification. Here, however, an integration time of 5000 ms was used, as the emission from the CO_2 plasma was low compared to the N_2 plasma emission. A spectrum along with the identified features is shown in figure 4.3.
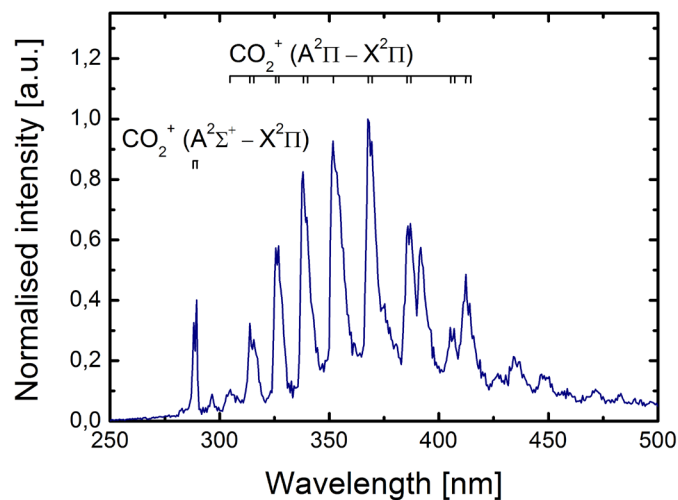
Figure 4.3: *This pure CO_2 spectrum was recorded using an applied frequency of 105 kHz and an integration time of 5000 ms. The peaks in the emission spectrum are mostly attributed to CO_2^+.*

Most of the dominant peaks in the CO_2 spectrum are attributed to the CO_2^+ Fox-Duffendack-Barker transition system ($A^2\Pi - X^2\Pi$). This system is known to occur in streaming CO_2. The first two peaks arise from another transition given by $A^2\Sigma^+ - X^2\Pi$. This transition is observed in almost all discharges containing CO_2 and the resulting bands are very persistent [20]. The only peak of high intensity that remains unknown is the one at 391 nm. While the other larger peaks are all identified, the origin of the structure beyond 425 nm is still unknown. The spectrum was checked

against any molecular species containing carbon and oxygen. Species containing nitrogen and hydrogen were also considered to account for a possible contamination of the system or an air leak. Some of the low intensity bands beyond 425 nm might match with peaks of lower intensity from the N_2 second positive system, the same that was observed earlier in the pure N_2 spectra. However, the higher intensity N_2 second positive system peaks are not visible in the CO_2 spectrum, although some peaks could coincide with the CO_2^+ bands. It should also be noted that the spectra for CO_2 were recorded with a 100 times longer integration time than those for N_2. This makes it unlikely that the N_2 second positive system is observed in the CO_2 emission spectrum. A higher resolution measurement could give a conclusive answer on the presence of N_2.

Mixtures of CO_2 and N_2

Besides recording the emission spectra of the pure gases, measurements were also made using a combination of CO_2 and N_2. The mixing ratios that were used are 5:1 and 1:1 (CO_2:N_2). For the 5:1 ratio the flow rates were approximately 0.24 L/min CO_2 and 0.05 L/min N_2 and for the 1:1 ratio the flow rates were approximately 0.22 L/min CO_2 and 0.24 L/min N_2. In figure 4.4 a spectrum measured at a gas ratio 5:1 is shown. It was measured with an integration time of 1500 ms. Figure 4.5 contains a spectrum at a gas ratio of 1:1 and was measured using an integration time of 500 ms. Both spectra were recorded using an applied frequency of 105 kHz.
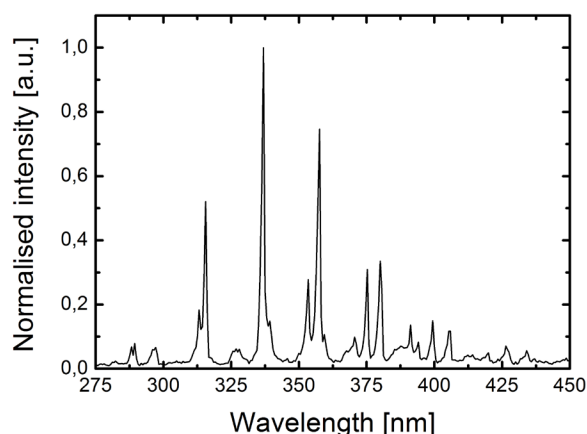
Figure 4.4: *The spectrum of CO_2 and N_2, at a mixing ratio of 5:1, measured using an integration time of 1500 ms.*
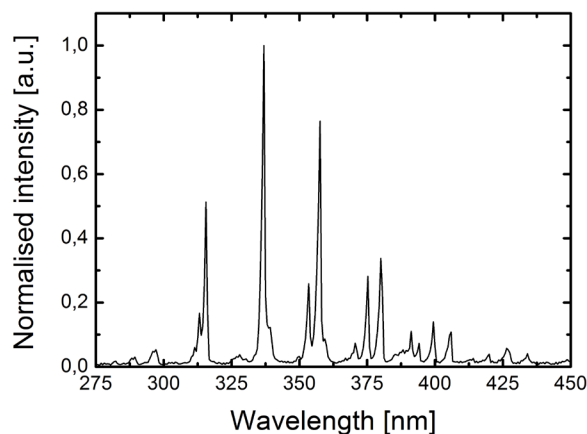
Figure 4.5: *The spectrum of CO_2 and N_2, at a mixing ratio of 1:1, measured using an integration time of 500 ms.*

Both spectra mainly resemble the features of a pure N_2 plasma. The spectrum at 1:1 mixing ratio shows similar intensity values to the 5:1 spectrum, but at a three times shorter integration time. That means that the light emitted from the 1:1 mixture ratio plasma is brighter. This is expected since the pure N_2 spectrum is much brighter than the pure CO_2 spectrum. Also in both spectra features that arise from CO_2^+ are detected. This is easily seen in figure 4.6, where a comparison between the normalised 5:1 and 1:1 mixture spectra, the pure N_2 spectrum and the pure CO_2 spectrum is shown. The CO_2^+ peaks have a higher (relative) intensity in the 5:1 spectrum than in the 1:1 spectrum, which is also expected, since the relative amount of CO_2 in the mixture is also higher. This increase of CO_2 in the mixture is most easily seen at 288 nm, where CO_2^+ causes two persistent peaks. No species other than those already identified in the pure emission spectra for N_2 and CO_2 are found in the mixtures.
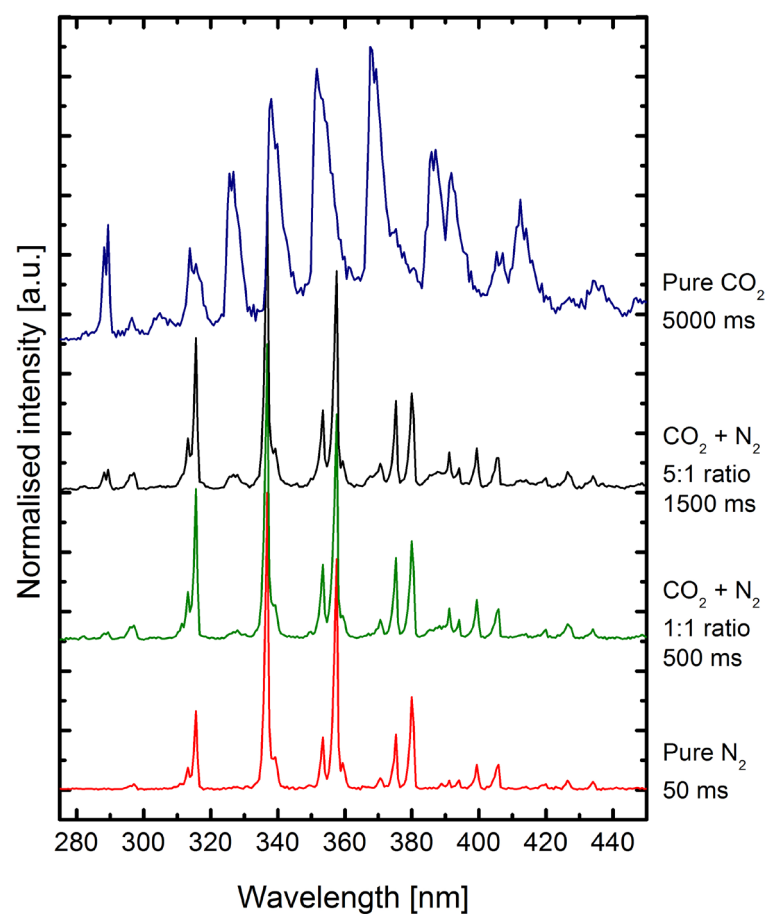
Figure 4.6: *From bottom to top a pure N_2 spectrum, the 1:1 mixing ratio spectrum, the 5:1 mixing ratio spectrum and a pure CO_2 spectrum are shown. The corresponding integration times are shown on the right side.*

4.2. Applied Power and Frequency Analysis

To assess the effect of amplitude and frequency of the applied voltage on the recorded spectra, the non-normalised emission spectra of pure CO_2 at different frequencies and powers are plotted in figure 4.7. The power values are calculated from Lissajous figures with about 20% accuracy.
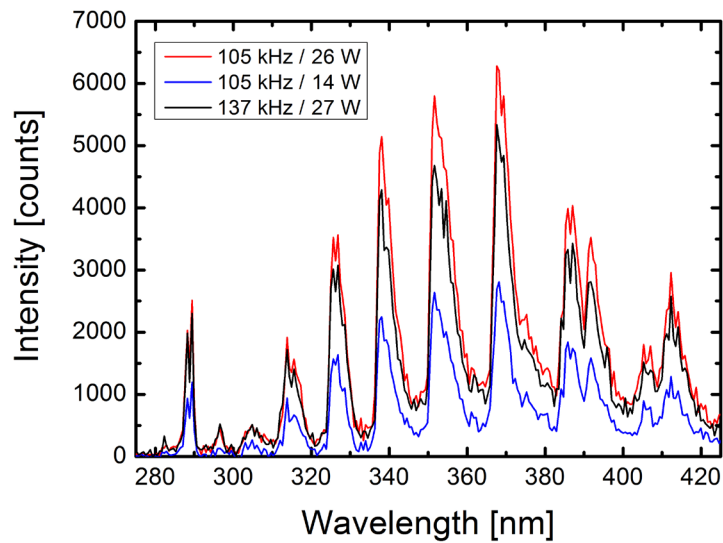
Figure 4.7: *All three pure CO_2 spectra were measured at the same integration time (5000 ms). The blue and the red spectra were measured at the same frequency, but using different power values. The red and the black spectra were measured at similar power values, but using different frequencies. The only difference is the intensity; the features of all three spectra are the same.*

The relative intensities and features of the different spectra remain the same for different applied frequencies and powers. So changing the applied frequency and power has no qualitative effects on the emission spectra. The same can be concluded from comparing other measurements for any of the gas mixtures. A total of 41 measurements were performed and the acquired data is summarised in the following tables. For each of the gas species and mixtures the intensity of the highest unsaturated peak is listed to compare the relative behaviour of different measurements. In most of the sub-tables the intensities roughly scale with the transferred power. However, there are some inconsistencies that will be further discussed in the next chapter.

Table 4.1: *Data of the 14 pure N_2 measurements. The counts for the peak at 379.98 nm are listed.*

Pure N_2

33.0 kHz			61.1 kHz		
Integration time [ms]	*Power [W]*	*Peak counts*	*Integration time [ms]*	*Power [W]*	*Peak counts*
50	12	1916	50	13	2540
100	9	3175	100	12	5588
100	13	5580	100	16	7980

105 kHz			137 kHz		
Integration time [ms]	*Power [W]*	*Peak counts*	*Integration time [ms]*	*Power [W]*	*Peak counts*
50	7	2133	25	11	1487
50	25	5562	25	33	4258
50	26	7802	50	8	2618
100	13	7360	50	25	6514

Table 4.2: *Data of the 7 pure CO_2 measurements. The counts for the peak at 367.60 nm are listed.*

Pure CO_2

33.0 kHz

Integration time [ms]	Power [W]	Peak counts
5000	13	836

61.1 kHz

Integration time [ms]	Power [W]	Peak counts
5000	14	1176
5000	17	1427

105 kHz

Integration time [ms]	Power [W]	Peak counts
5000	14	1539
5000	26	3429

137 kHz

Integration time [ms]	Power [W]	Peak counts
5000	7	1237
5000	27	2914

Table 4.3: *Data of the 10 CO_2 and N_2 mixture measurements at a ratio of 5:1. The counts for the peak at 379.98 nm are listed.*

CO_2 + N_2
Mixing ratio 5:1

33.0 kHz

Integration time [ms]	Power [W]	Peak counts
3000	9	3259

61.1 kHz

Integration time [ms]	Power [W]	Peak counts
2000	16	2692
3000	12	2574
3000	17	4123

105 kHz[1]

Integration time [ms]	Power [W]	Peak counts
1500	21	6413
1500	33	3929

137 kHz

Integration time [ms]	Power [W]	Peak counts
1500	19	2762
1500	26	5072
2000	17	3225
2000	31	6306

---

[1] The power values and intensities (count numbers) in this table suggest that an approximately 61% higher intensity was obtained while only 64% of the power was coupled into the plasma. This inconsistency is most probably due to an inaccurate power calculation from bad oscilloscope data.

Table 4.4: *Data of the 10 CO$_2$ and N$_2$ mixture measurements at a ratio of 1:1. The counts for the peak at 379.98 nm are listed.*

**CO$_2$ + N$_2$
Mixing ratio 1:1**

33.0 kHz

Integration time [ms]	Power [W]	Peak counts
3000	9	6810

61.1 kHz

Integration time [ms]	Power [W]	Peak counts
500	16	1497
1500	11	2460
1500	20	6408

105 kHz

Integration time [ms]	Power [W]	Peak counts
500	25	4089
1500	20	6503
1500	29	11266

137 kHz

Integration time [ms]	Power [W]	Peak counts
500	36	3778
1500	6	3719
1500	37	10434

5. Discussion

First the species in the pure N_2 and CO_2 emission spectra were identified. Emission from N_2 and N_2^+ transitions were observed in pure N_2 DBDs. All the peaks could be identified. In the lower wavelength region traces of NO were found. The origin of the NO is still unclear, but possible explanations include a leak in the system or contamination of the N_2 gas.

Most of the dominant peaks in the spectra recorded from pure CO_2 plasmas were identified as CO_2^+, while the identity of the lower intensity structures beyond 425 nm is still unknown. One peak of high intensity at 391.76 nm also remained unidentified. This peak was however also measured in CO_2 by Mrozowski [21] and later assigned to the CO_2^+ sub-band $^2\Pi_{3/2}$ - $^2\Pi_{3/2}$ by Johns [22]. Von Horst also measured the emission spectra of N_2 and CO_2, albeit at lower pressures ranging from 5 up to 200 Torr [23]. The peaks in those spectra at 200 Torr closely resemble the features of the spectra in this work and the same identifications were made for both N_2 and CO_2. In von Horst's previous study, the peaks beyond 425 nm in the CO_2 emission spectrum also remain unknown. While no CO was identified in the emission spectra, it could still be present. This would imply that it is either not electronically excited or its emission is very low compared to CO_2^+.

The emission from the CO_2 plasma was very weak in the visible and UV range and hence long integration times were required. This also resulted in relative high noise levels. The weak emission will make it challenging to record spectra with higher spectral resolution or time-resolved spectra. The low emission could indicate a low energy loss through radiative relaxation processes of electronically excited states, which is desirable in terms of energy efficiency. However, it is important to note that no conclusion about the efficiency can be drawn from this information alone. Other processes occurring in the plasma and their outcomes will have to be studied first.

Changing the frequency and power of the applied voltage had no qualitative effects on the emission spectra. From the measurements the intensity seems to scale with the injected power at a given frequency for each of the gas mixtures. There are some inconsistencies however, as was mentioned in table 4.3. Those inconsistencies are most likely caused by inaccuracies in the scope data and the intrinsic inaccuracy of the used high voltage determination. More accurate power measurements using a high voltage probe are essential in the future. The Lissajous figures were used because there was no high voltage probe available. Heat dissipation in the system and parasitic discharges outside the reactor proved another challenge, especially when longer integration times were required as in the case of pure CO_2.

6. Summary

The process limiting step in the (solar powered) conversion of CO_2 is known to be the dissociation of CO_2. High dissociation energy efficiencies are reported for non-equilibrium plasmas [2]. Therefore a dielectric barrier discharge (DBD) is considered to effectuate the dissociation. The goal of this project was to set up an in-situ optical diagnostic and to analyse the emission spectra originating from the plasma. Optical emission spectroscopy (OES) was used on an atmospheric pressure DBD in CO_2, N_2 and mixtures of these two gases to characterise a new setup and to prepare further studies on the plasma-assisted dissociation of CO_2. Two spectrometers were used and calibrated: this involved both spectral calibration as well as relative intensity calibration using a tungsten ribbon lamp. The identities of the electronically excited species present in the plasma were determined by comparing the measured spectra with literature. The effect of the applied voltage and frequency was studied by mutual comparison of the spectra.

The dominant peaks in the emission spectra of pure CO_2 were attributed to CO_2^+, while the origin of the lower intensity bands in the region above 425 nm is still unknown. In the pure N_2 emission features of N_2, N_2^+ and NO were observed. When CO_2 was mixed with N_2, the N_2 emission bands remain dominant in the spectrum. Changing the applied voltage amplitude and frequency did not have any qualitative influences on the emission spectra.

7. Outlook

Optical emission spectroscopy could in the future be further used to determine plasma parameters such as the vibrational temperature. To do so, the vibrational states have to be assigned to their corresponding peaks in a calibrated spectrum. The temperature can then be obtained from the slope of a Boltzmann plot. The calibration itself can be improved by using a UV source instead of the tungsten ribbon lamp, as the CO_2 emission is mainly in UV region. Using an ICCD camera (intensified charge-coupled device camera) time resolved spectra can be measured. However, the weak optical emission from DBDs in pure CO_2 might prove to be a challenge when using an ICCD camera.

While with OES only excited species are detected, absorption spectroscopy could be used to identify ground state species. This could be achieved with in-situ Fourier-transform infrared (FTIR) spectroscopy for example, which gives access to vibrational and rotational transitions. By doing ex-situ FTIR measurements the dissociation rates could also be determined. Vibrational pumping is an important principle to achieve high dissociation efficiencies in the conversion process, it may therefore also be interesting to research the vibrational excitations of the molecules using Raman spectroscopy.

References

Literature

[1] N. Lewis and D. Nocera, *Proc. Natl. Acad. Sci.,* **35**, 15729 (2006).

[2] A. Fridman, *"Plasma Chemistry,"* Cambridge: Cambridge Universiy Press (2008).

[3] Energy Information Administration, *"Annual Energy Outlook 2011,"* US Dept. of Energy, Washington, DC (2011).

[4] National Academy of Sciences, *"Understanding and Responding to Climate Change,"* (2008) [Online]. Available: http://dels-old.nas.edu/dels/rpt_briefs/climate_change_2008_final.pdf. [Accessed 2 January 2012].

[5] W. Chueh, C. Falter, M. Abbott, D. Scipio, P. Furler, S. Haile and A. Steinfeld, *Science*, **330**, 1797 (2010).

[6] Koninklijk Nederlands Meteorologisch Instituut (KNMI), *"Zonnestraling in Nederland,"* [Online]. Available: http://www.knmi.nl/bibliotheek/knmipubDIV/Zonnestraling_in_Nederland.pdf. [Accessed 21 03 2012].

[7] O. Varghese, M. Paulose, T. LaTempa and C. Grimes, *Nano Letters,* **9**, 731 (2009).

[8] U. Kogelschatz, *Plasma Chemistry and Plasma Processing,* **23**, 1 (2003).

[9] P. Atkins and J. de Paula, *"Physical Chemistry,"* Oxford: Oxford University Press (2006).

[10] W. Demtröder, *" Atoms, Molecules and Photons,"* Berlin: Springer, 2006.

[11] T. Engel, *"Quantum Chemistry & Spectroscopy,"* San Francisco: Pearson (2006).

[12] P. Sindhu, *"Elements of Molecular Spectroscopy,"* Kent: New Age Science (2009).

[13] R. Robinett, *"Quantum Mechanics,"* Oxford: Oxford University Press (2006).

[14] A. Eletskii and B. Smirnov, *Pure & Appl. Chem.,* **57**, 1235 (1985).

[15] G. Willis, W. Saryend and D. Marlow, *J. Appl. Phys.,* **50**, 68 (1969).

[16] V. Legasov, V. Rusanov and A. Fridman, *Plasma Chem.,* **5**, 116 (1978).

[17] S. Starostin, P. Premkumar, M. Creatore, E. van Veldhuizen, H. de Vries, R. Paffen and M. van de Sanden, *Plasma Sources Sci. Technol.,* **18**, 45021 (2009).

[18] A. Fridman, A. Chirokov and A. Gutsol, *J. Phys. D: Appl. Phys.,* **38**, R1 (2005).

[19] T. Manley, *Trans. Electrochem. Soc.,* **84**, 83 (1943).

[20] R. Pearse and A. Gaydon, *"The Identification of Molecular Spectra,"* London: Chapman and Hall (1984).

[21] S. Mrozowski, *Physical Review,* **72**, 682 (1947).

[22] J. Johns, *Canadian Journal of Physics,* **64**, 1004 (1964).

[23] A. von Horst, *Annalen der Physik,* **7**, 178 (1966).

[24] Ocean Optics, Inc., *"USB2000 Fiber Optic Spectrometer, Installation and Operation Manual,"* 2005. [Online]. Available: http://www.oceanoptics.com/technical/USB2000%20Operating%20Instructions.pdf. [Accessed 31 October 2011].

[25] National Institute of Standards and Technology, *"NIST Atomic Spectra Database,"* September 2010. [Online]. Available: http://nist.gov/pml/data/asd.cfm. [Accessed 1 November 2011].

[26] National Physical Laboratory, *"Certifcate of Calibration: Tungsten Ribbon lamp, gas filled No. P300C,"* Teddington Middlesex, UK (2010).

[27] J. de Vos, *Physica,* **20**, 715 (1954).

[28] J. de Vos, *Physica,* **20**, 690 (1954).

[29] J. Janin, *C. R. Acad. Sci.,* **207**, 145 (1938).

List of Figures

List of Tables

Appendix A: Spectrometer Calibration

A1. Wavelength Calibration

To perform the wavelength calibration of the Ocean Optics USB 2000 spectrometer, four gas-discharge lamps were used: a helium lamp, a mercury lamp, a sodium lamp and a zinc lamp. The measured spectra were used to match each pixel of the sensor with its correct wavelength value. To calibrate the spectrometer the following equation, which shows the relationship between pixel-number and wavelength, had to be solved [24]:

$$\lambda_p = I + C_1 p + C_2 p^2 + C_3 p^3 \tag{A1-1}$$

In equation A1-1 λ_p is the wavelength of pixel number p, I the wavelength of pixel number 0 (the first pixel) and C_1, C_2 and C_3 are calibration coefficients. By measuring the known spectra of the gas-discharge lamps and using a third-order linear regression, the coefficients could be calculated. The wavelength of a particular pixel then matches the actual wavelength within the optical resolution. In table A.1 the pixel numbers and their corresponding wavelengths are shown. The Atomic Spectra Database by the National Institute of Standards and Technology [25] was used as reference for the wavelength values of the atomic spectral lines. The calculated values are shown in table A.2 and were programmed into the spectrometer's EEPROM (Electrically Erasable Programmable Read-Only Memory).

Table A.1: *In the first column the element present in the lamp is stated. The second column shows the value of the spectral lines observed from that particular element. The third column contains the pixel number at which the spectral line was measured.*

Table A.2: *Using a linear regression the calibration constants are calculated from the data in table A.1. The values listed in this table were programmed into the spectrometer's EEPROM.*

Element	Wavelength [nm]	pixel #
Helium (He)	388,86	563
	447,14	724
	501,56	877
	587,56	1125
	667,81	1366
	706,51	1485
Sodium (Na)	588,99	1131
Zinc (Zn)	468,01	782
	472,22	794
	481,05	819
	636,23	1270
Mercury (Hg)	365,02	498
	404,65	606
	435,83	692
	546,08	1004
	579,07	1100

Calibration constant	Value
I [nm]	$1.7637224 \cdot 10^2$
C_1 [nm/pixel]	$3.8847500 \cdot 10^{-1}$
C_2 [nm/pixel^2]	$-1.8491450 \cdot 10^{-5}$
C_3 [nm/pixel^3]	$-1.8295920 \cdot 10^{-9}$

A2. Relative Intensity Calibration

The optics in the setup and inside any spectrometer have wavelength dependent transmission characteristics. This means that different wavelengths will also be filtered differently and this leads to incorrect (relative) intensities in the measured spectrum. To obtain a spectrum with calibrated relative intensities I_C a correction has to be made to the measured spectrum I_M. Strictly speaking, such a calibration has to be performed for every emission spectrometer and is carried out with a calibrated source. The relation between the measured (I_M) and the calibrated (I_C) intensities can be simply expressed as:

$$I_C = K(\lambda)I_M ,$$
(A2-1)

where $K(\lambda)$ is the wavelength dependent correction function. To obtain this function, a light source with known spectral density is required. A tungsten ribbon lamp with a single window, cylindrical envelope and 1.3 mm wide filament (lamp identification number: P300C) is used for this purpose [26]. The emission spectrum of the tungsten ribbon lamp I_C can theoretically be described as the spectrum of a grey-body radiator I_{GB}. A grey-body radiator is related to a black-body radiator I_{BB} by equation A2-2 [27].

$$I_C = I_{GB}(\lambda,\theta) = \tau\varepsilon(\lambda,\theta)I_{BB}(\lambda,\theta)$$
(A2-2)

The temperature is denoted by θ. On the right-hand side, τ is the transmission factor, which is determined by the type of glass that is used in the tungsten ribbon lamp, and ε is the emissivity of tungsten. The used tungsten ribbon lamp has a transmission factor τ = 0.92 and the emissivity of tungsten can be found in literature [28]. I_{BB} is known from Planck's law for black-body radiators [10], [27]:

$$I_{BB}(\lambda,\theta) = \frac{2hc^2}{\lambda^5}\frac{1}{\exp\left(\dfrac{hc}{\lambda k\theta}\right)}$$
(A2-3)

To calculate the grey-body intensity the <u>true temperature T</u> of the tungsten ribbon lamp is required in the above mentioned equation(s). The true temperature T of a source is the temperature as measured by a suitable thermometer in thermal equilibrium with the source. In the case of black-body radiation, the true temperature T is the temperature for which Planck's equation (A2-3) accurately resembles the **global spectral radiance**.

In practise, the manufacturer of the lamp specifies only the <u>radiation temperature S</u> for several operation currents, whereas the true temperature, T, is *a priori* unknown. The radiation temperature S of a source is the temperature of an ideal black-body radiator that has the same radiance at a **specified wavelength**, λ_0. It is essential to understand the difference between these two temperatures to avoid severely damaging the calibration source, as $T > S$. Since the manufacturer only provides a list of radiation temperatures for certain currents, the spectral density of the tungsten ribbon lamp has to be calculated by means of equation A2-2. As mentioned, this step requires the true temperature the intensity of the equivalent black-body radiation $I_{BB}(\lambda,T)$. It is therefore first necessary to first calculate the true temperature T from the radiation temperature S.

The true temperature can be approximated by a two-step iteration process. For wavelength λ_0, at which the radiation temperature S is given, equation A2-2 becomes [27]:

$$I_{BB}(\lambda_0,S) = \tau\varepsilon(\lambda_0,T)I_{BB}(\lambda_0,T) \qquad (A2\text{-}4)$$

The procedure to approximate the true temperature T is as follows:

1. Calculate $I_{BB}(\lambda_0,S)$.

2. From equation A2-4 $I_{BB}(\lambda_0,T)$ can be calculated

   $$I_{BB}(\lambda_0,T) = \frac{I_{BB}(\lambda_0,S)}{\tau\varepsilon(\lambda_0,T)}.$$

   However, $\varepsilon(\lambda_0,T)$ is still unknown, so $\varepsilon(\lambda_0,S)$ is used as first order approximation, which leads to an estimate of the true temperature $T^{(1)}$

   $$I_{BB}(\lambda_0,T^{(1)}) = \frac{I_{BB}(\lambda_0,S)}{\tau\varepsilon(\lambda_0,S)}.$$

3. When the result $I_{BB}(\lambda_0,T^{(1)})$ from step 2 is inserted into Planck's equation (A2-3), $T^{(1)}$ can be calculated and subsequently $\varepsilon(\lambda_0,T^{(1)})$ can be obtained.

4. The second approximation of the true temperature $T^{(2)}$ can be calculated using the results from step 3

   $$I_{BB}(\lambda_0,T^{(2)}) = \frac{I_{BB}(\lambda_0,S)}{\tau\varepsilon(\lambda_0,T^{(1)})}.$$

Since the emissivity of tungsten is a rather slowly changing function of the temperature, the second approximation is in practise usually very close to the true temperature: $T \approx T^{(2)}$ [27].

In figure A.1 the measured tungsten ribbon lamp spectrum and the calculated theoretical spectrum are shown. The tungsten ribbon lamp spectrum was recorded at a radiation temperature of S = 2513 K, which corresponds to a true temperature of T = 2820 K. The radiation temperature was provided for wavelength λ_0 = 658.4 nm.
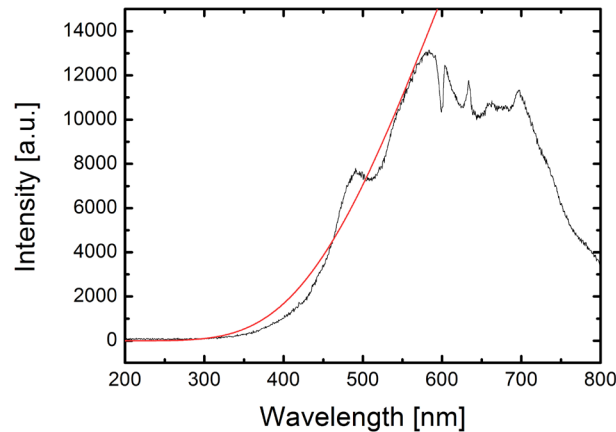

Figure A.1: *The measured tungsten ribbon lamp spectrum (black) and the theoretical grey-body spectrum (red).*

Next, the function $K(\lambda)$, as defined in equation A2-1, is obtained from a comparison between the measured tungsten ribbon spectrum I_{TR} (= I_M) and the calculated grey-body spectrum I_{GB} (= I_C). K(λ) follows from equations A2-5 and A2-6:

$$I_{GB}(\lambda,T) = \frac{I_{GB}(\lambda,T)}{I_{TR}}I_{TR} = \frac{\tau\varepsilon(\lambda,T)I_{BB}(\lambda,T)}{I_{TR}}I_{TR} = K(\lambda)I_{TR} \qquad \text{(A2-5)}$$

$$K(\lambda) = \frac{\tau\varepsilon(\lambda,T)I_{BB}(\lambda,T)}{I_{TR}} \approx \frac{\tau\varepsilon(\lambda,T^{(2)})I_{BB}(\lambda,T^{(2)})}{I_{TR}} \qquad \text{(A2-6)}$$

From figure A.1 it can be seen that the intensities of both spectra are low in the lower wavelength regions. Hence, the ratio between I_{GB} and I_{TR} will lead to amplification of the noise from the measured spectrum in this spectral range. This reduces the quality of the correction function, as shown in figure A.2 by the black graph:
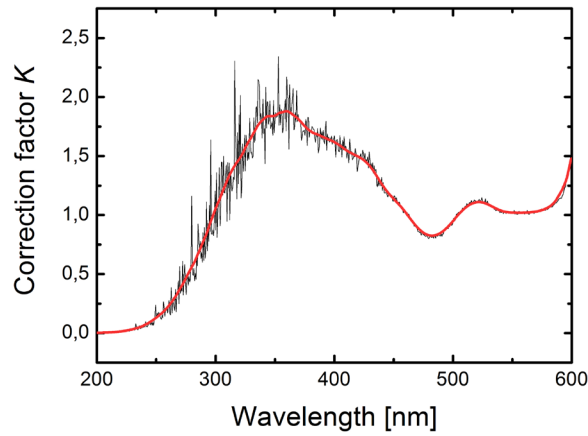

Figure A.2: *The straightforwardly calculated correction function (black) and the correction function after adjacent averaging (red).*

Adjacent averaging is applied to smooth the correction function using a 'window' consisting of 42 data points. If the correction function is not smoothened it will introduce incorrect new peaks in a measured spectrum. The result from this smoothing process, the red line figure A.2, is applied to the measured spectra to obtain spectra with correct relative intensities.

Appendix B: Identification of Emission Spectra

In chapter 4 a general outline of the identification process was given. This appendix provides a more extensive explanation to the identification of molecular spectra. The identification of the species in pure CO_2 plasma and the pure N_2 plasma are discussed.

For both plasmas the following procedure was used: first the wavelength values of the emission peaks in the spectra were determined and checked against a list of persistent band heads from literature to get an indication of which species and transitions to further investigate [20]. The suggested transitions are then visually compared with the measured spectrum to determine its presence. ´The identification of molecular spectra´ by Pearse & Gaydon [20] is used as source for the spectra of the transition systems unless mentioned otherwise.

B1. Pure N_2 Plasma

A pure N_2 plasma spectrum was measured using a sinusoidal voltage with a frequency of 105 kHz and a integration time of 50 ms. The intensities were normalised to the maximum value. The resulting spectrum is shown in figure B.1.
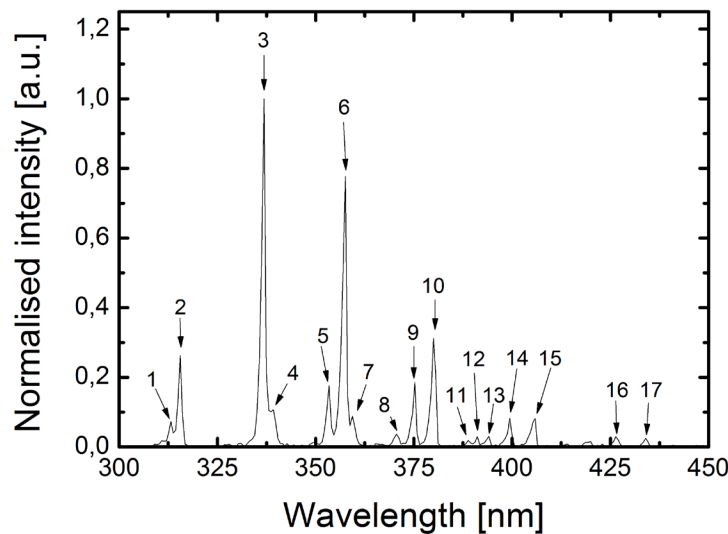

Figure B.1: *The spectrum of a DBD in pure N_2 at atmospheric pressure measured using an integration time of 50 ms.*

The peaks of the spectrum in figure B.1 were numbered and their corresponding wavelength values are summarised in table B.1. If a peak coincides with a persisting head, the wavelength value of the head is displayed in the third column, along with the transition system associated with the head. The peak wavelengths were checked against persistent heads for molecular species containing nitrogen, hydrogen and oxygen to take the possibilities of water contamination and an air leak in the system into account.

Table B.1: *The peak wavelengths are checked against known coinciding persistent heads to get an indication of the possibly present species. The transition systems in the last column are suggestions and <u>not</u> definitive matches.*

Peak #	Wavelength [nm]	Coinciding head [nm]	Suggested transition system
1	313.18		
2	315.55	315.93	$N_2 - 2^{nd}$ pos.
3	336.88	337.13	$N_2 - 2^{nd}$ pos.
4	339.25		
5	353.45		
6	357.57	357.69	$N_2 - 2^{nd}$ pos.
7	359.34		
8	370.55	370.62	$N_2 -$ Goldstein-K.
9	375.27		
10	379.98	380.49	$N_2 - 2^{nd}$ pos.
11	388.81		
12	391.17	391.44	$N_2^+ - 1^{st}$ neg.
13	394.11		
14	399.40		
15	405.87	405.94	$N_2 - 2^{nd}$ pos.
16	426.40		
17	434.02	434.36	$N_2 - 2^{nd}$ pos.

The table shows that only N_2 and N_2^+ transitions coincide the measured peak wavelengths. To confirm an actual match the transition systems are now fully compared with the measured spectrum. The second positive system is found multiple times and is therefore further investigated first. The spectrum of the N_2 second positive system is in shown in figure B.2 together with the measured spectrum.
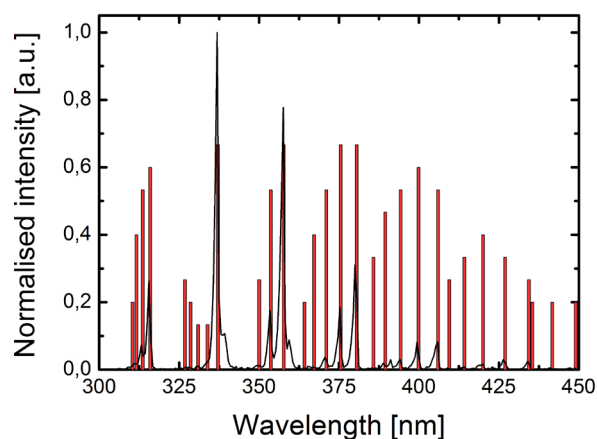

Figure B.2: *The measured spectrum (black line) compared with the N_2 second positive transition system (red bars).*

The bars of the second positive system figure B.2 match with all the peaks and bands in the spectrum except for peaks 4, 7 and 12. The difference in relative intensities can be explained by the different plasma conditions of the reference measurement. Different conditions can lead to a different energy distribution and population of vibrational levels [10].

Peak number 12 in figure B.1 did not match with any of the N_2 second positive system peaks in figure B.2. However, this peak did coincide with a persistent head of the N_2^+ first negative system, as was stated in table B.1. So the N_2^+ first negative system is compared to the measured spectrum next. An enlarged view of the system is shown in figure B.3. The intensity of the reference spectrum is scaled down for easier comparison.
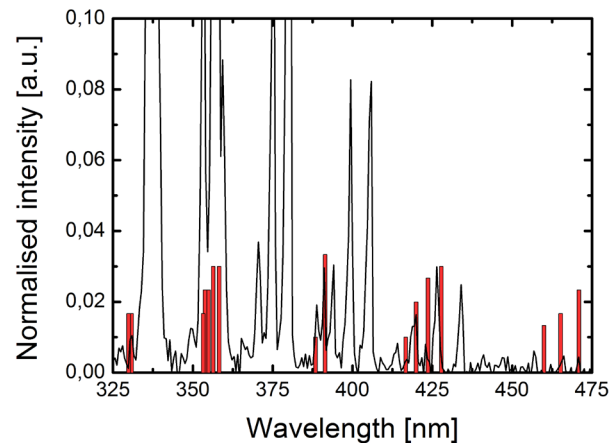

Figure B.3: *The measured spectrum (black line) compared with the N_2^+ first positive transition system (red bars).*

The bars in figure B.3 just above 350 nm are overlapping too much with the more intense N_2 second positive system to confirm a match, but all the other bars coincide with the peaks of lower intensity. So the N_2^+ first negative system is expected to present, albeit to a much lesser extent than the N_2 second positive system discussed earlier.

Lastly, the Goldstein-Kaplan system is compared to the measured spectrum in figure B.4. There is little resemblance between the two spectra as most the reference peaks do not match with peaks of the measured spectrum.
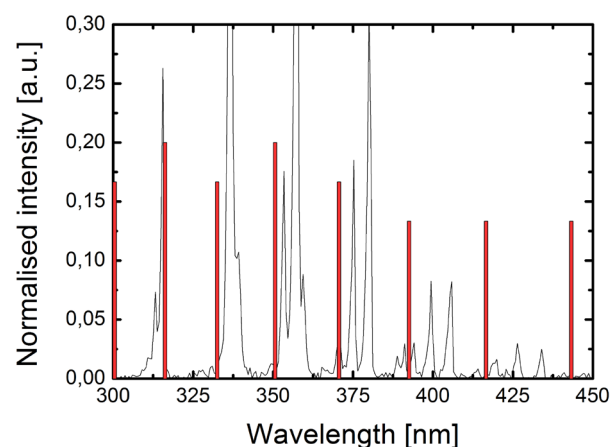

Figure B.4: *The measured spectrum (black line) compared with the N_2 Goldstein-Kaplan transition system (red bars).*

Concluding, the pure N_2 plasma emission spectrum can be mostly attributed to the N_2 second positive transmission system. The N_2^+ first negative transition system is also observed but to a lesser extent.

B2. Pure CO₂ Plasma

A pure CO_2 plasma optical emission spectrum was measured using an applied frequency of 105 kHz and an integration time of 5000 ms. The intensities were normalised to the maximum value. The resulting spectrum is shown in figure B.5.
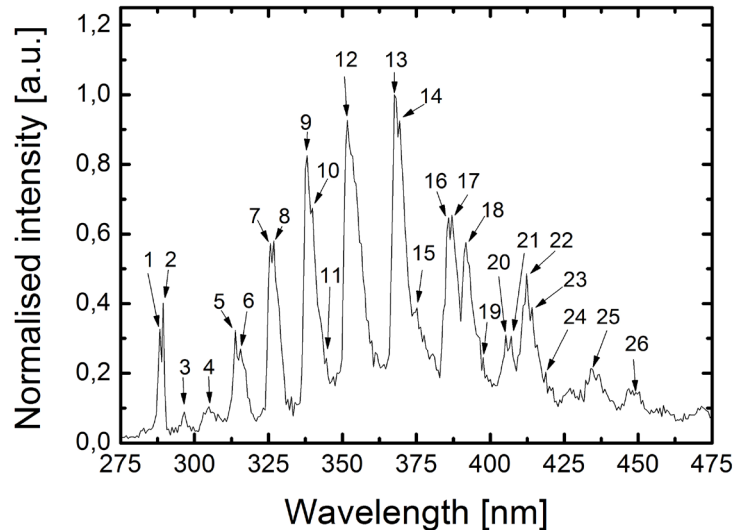

Figure B.5: *The spectrum of a pure CO_2 plasma measured using an integration time of 5000 ms.*

The peaks of the spectrum in figure B.5 were numbered and their corresponding wavelength values, coinciding heads and the associated transitions systems are shown in table B.2. The same procedure as for the N_2 spectrum is used: the peak wavelengths were checked against persistent heads for molecular species containing carbon, oxygen, nitrogen and hydrogen to also take the possibilities of water contamination and an air leak in the system into account. In addition to the transition systems in table B.2, different systems of CO, O_2, CN, OH and their ions were also checked for similar plasma conditions. However, the only matching system was the CO_2^+ Fox-Duffendack-Barker system. The CO_2^+ Fox-Duffendack-Barker system is compared with the measured spectrum in figure B.6. Some of smaller peaks, in particular peak 3 and 26, coincide with the peaks of the N_2 second positive system. The comparison for the N_2 second positive system is shown in figure B.7.

Table B.2: *The peak wavelengths are checked against known coinciding persistent heads to get an indication of the possibly present species. The transition systems in the last column are suggestions and <u>not</u> definitive matches.*

| Peak #	Wavelength [nm]	Coinciding head [nm]	Suggested transition system
1	288.24		
2	289.42		
3	296.56		
4	304.87	304.36	O_2^+ - 2nd neg.
5	313.78	313.74 / 313.44	O_3 / CO - 3rd pos.
6	315.55	315.93	N_2 - 2nd pos.
7	325.63		
8	326.82		
9	338.07		
10	339.84	339.78	O_2^+ - 2nd neg.
11	344.57		
12	351.66	351.7	O_2 - Schumann-R.
13	367.6	367.1	O_2 - Schumann-R.
14	369.37		
15	375.27		
16	385.87		
17	387.05	387.05	CO_2^+ - Fox-D.-B.
18	391.76		
19	397.64	397.77	CO^+ - Baldet-J.
20	405.28		
21	407.04		
22	412.32	412.48	CO - Herzberg
23	414.09		
24	418.78		
25	434.02	434.36	N_2 - 2nd pos.
26	448.06	448.0	
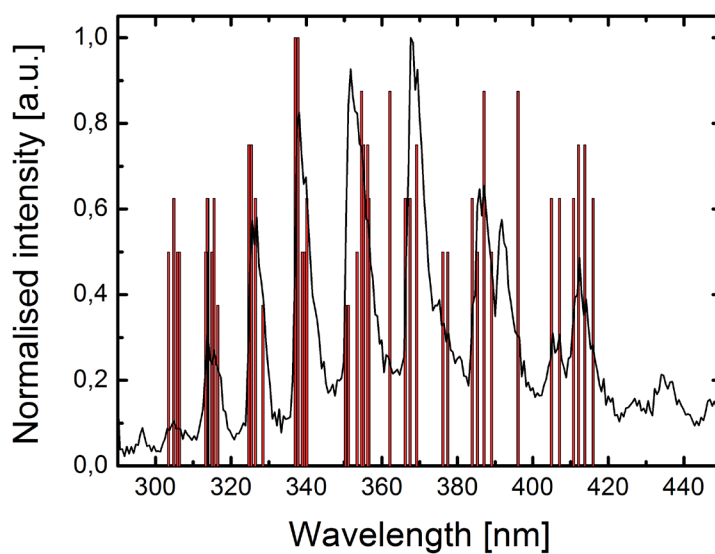
Figure B.6: *The measured spectrum (black line) compared with the CO_2^+ Fox-Duffendack-Barker system (red bars).*
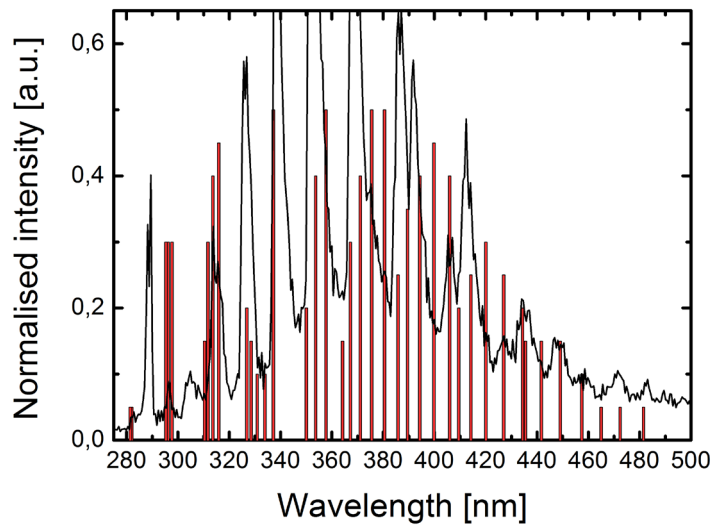
Figure B.7: *The measured spectrum (black line) compared with the N_2 second positive transition system (red bars).*

From figure B.6 is concluded that the dominant peaks originate from the CO_2^+. While some of the smaller peaks might match with the N_2 second positive system in figure B.7, most of the larger N_2 peaks are absent. Using integration times of 5000 ms, the N_2 second positive system peaks are also expected to be more dominant if present. This makes it unlikely that the N_2 second positive system is observed.

The first two to peaks arise from a CO_2^+ transition that is very persistent in discharge tubes containing CO_2^+ are illustrated in figure B.8. The only peak of larger intensity that remains unidentified is the peak at 391.76 nm. From further literature study it is fond that this peak was also measured in CO_2 by Mrozowski [21] and later assigned to the CO_2^+ sub-band $^2\Pi_{3/2}$ - $^2\Pi_{3/2}$ by Johns [22].

For completeness, the other transition systems, mentioned in table B.2 but that did not match the measured spectrum, are compared with the measured spectrum in figures B.9 through B.14.
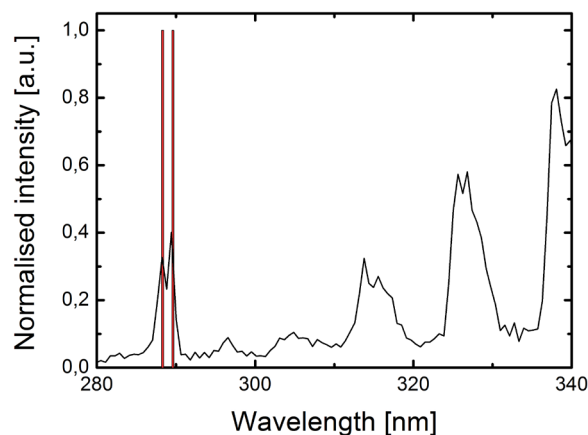

Figure B.8: *The measured spectrum (black line) compared with the persistent CO_2^+ bands at 288.3 nm and 289.6 nm (red bars).*
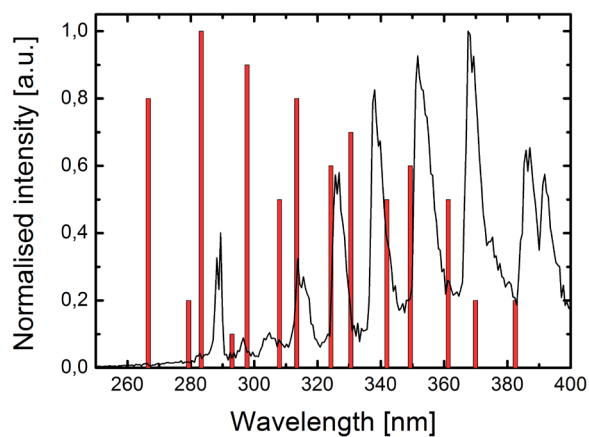
Figure B.9: *The measured spectrum (black line) compared with the CO third positive transition (red bars).*
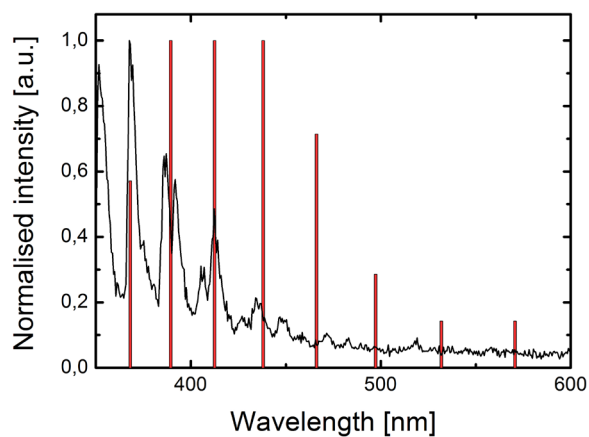

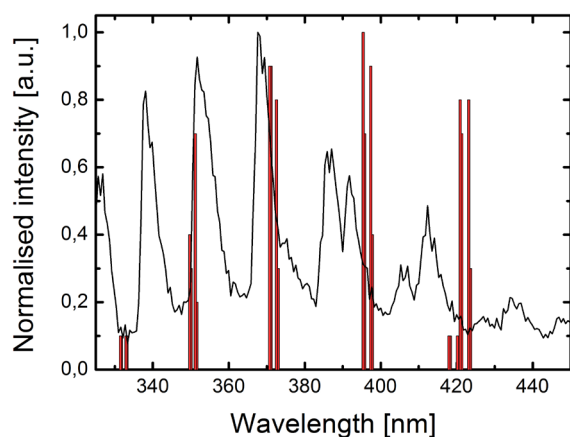**Figure B.10:** *The measured spectrum (black line) compared with the CO Herzberg transition system (red bars).*

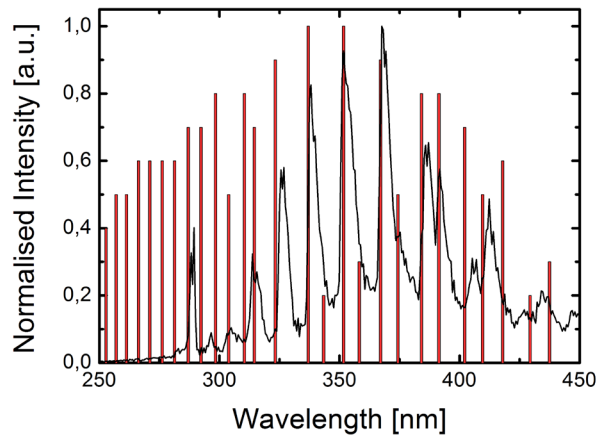**Figure B.11:** *The measured spectrum (black line) compared with the CO_2^+ Baldet-Johnson transition system (red bars).*

Figure B.12: *The measured spectrum (black line) compared with the O_2 Schumann-Runge transition system (red bars).*
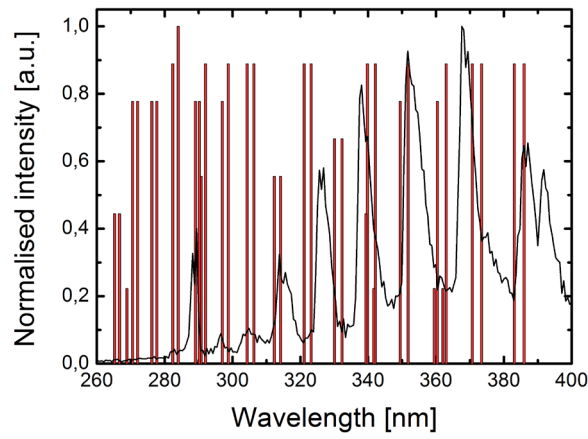

Figure B.13: *The measured spectrum (black line) compared with the O_2^+ second negative transition system (red bars).*
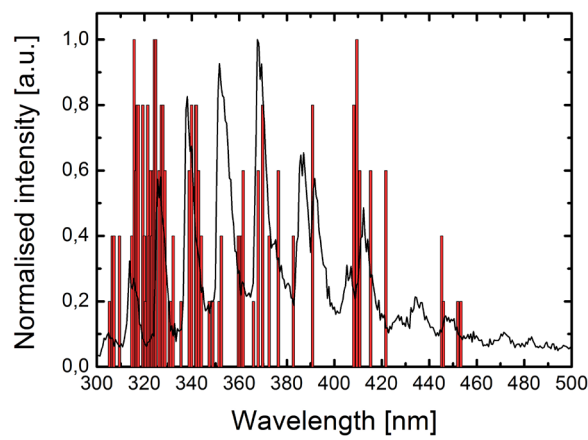

Figure B.14: *The measured spectrum (black line) compared with the O_3 Ultraviolet transition system (red bars). The intensity values of the O_3 spectrum were measured by J. Janin [29].*